CrossMark

ORIGINAL PAPER: NANO-STRUCTURED MATERIALS (PARTICLES, FIBERS, COLLOIDS, COMPOSITES, ETC.)

Green solvent-based sol–gel synthesis of monticellite nanoparticles: a rapid and efficient approach
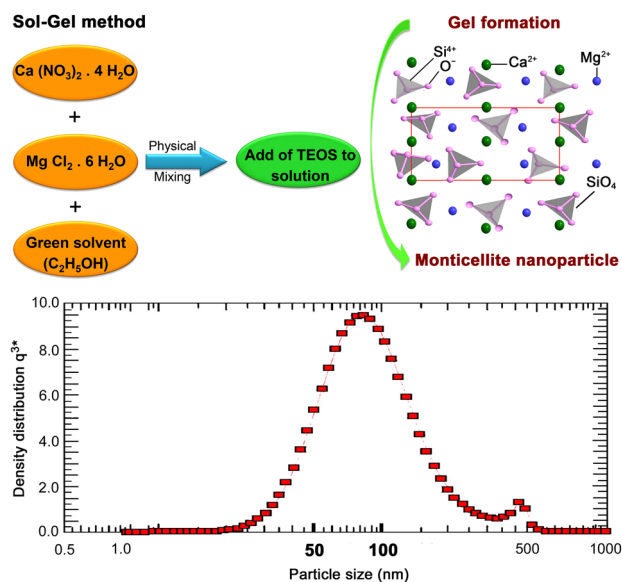
Erfan Kalantari[1,2] · Seyed Morteza Naghib[1] · M. Reza Naimi-Jamal[2] ·
Masoud Mozafari[3]

Abstract In this research, high-pure monticellite ceramic ($CaMgSiO_4$) nanoparticles were synthesized via a novel sol–gel method using ethanol and chloride ions for the acceleration of polycondensation process. The gel obtained from metal alkoxide and metal salts precursors dried at 100°C; then, the dried-gel calcined at different temperatures to monitor the structural development of the final samples. The effect of various heat-treatment temperatures on the x-ray diffraction patterns, followed by the calculations from scherrer's equation, showed that the grain size of the synthesized samples at 1200°C was around 28 nm. Based on dynamic light scattering spectroscopy, the size of most of the particles was ~85 nm. Williamson–Hall formula was also used to calculate the lattice strain of the samples. According to the results, by changing the heat-treatment temperature, lattice strain/stress, lattice parameters and grain size have meaningfully changed. The proposed synthesis method showed superior advantages in comparison with the other conventional techniques presented in the literature, which is relatively faster at lower temperatures. The synthesized high-pure monticellite nanoparticles could be applied in different biomedical engineering applications in which the purity and structural properties are of importance, such as dental, bone tissue engineering, coatings on biomedical implants, surgery hemostasis and inducing osteogenesis in vivo applications.

Graphical abstract

✉ Erfan Kalantari
kalantari.erfan@yahoo.com

✉ Seyed Morteza Naghib
naghib@iust.ac.ir

1   Nanotechnology Department, School of New Technologies, Iran University of Science and Technology (IUST), Tehran, Iran

2   Research Laboratory of Green Organic Synthesis and Polymers, Department of Chemistry, Iran University of Science and Technology (IUST), Tehran, Iran

3   Bioengineering Research Group, Nanotechnology and Advanced Materials Department, Materials and Energy Research Center (MERC), Tehran, Iran

Keywords Monticellite nanoparticles · Sol–gel method · Ethanol · Chloride ions · Crystal structure

1 Introduction

Development of bioceramics is a critical goal for many relevant biomedical applications [1–5]. Favorable ion

transportation capability of bioceramics has attracted bio-medical engineers to develop novel synthetic routs for multifunctional applications mainly in hard tissue engineering [6–9]. Further characteristics including mechanical strength, toughness, and creep behavior of bioceramics play a key role in the development of materials and composites for using in load-bearing regions of the body [7]. As a conventional bioceramic, sintered hydroxyapatite (HA) has been previously used in many biomedical applications due to its physicochemical properties and biological affinity such as its close similarity with the inorganic part of hard tissues that confer biocompatibility and ability to permit new bone formation and adhesion [10–12]. During the last few years, different magnesium-containing bioceramics have been proposed for advanced biomedical applications mainly in dental and bone tissue engineering. It is known that there are important elements in the human body such as magnesium (mostly in bone tissues), which is essential for the health, strength, and firmness of bones [13]. Recent studies have shown an increase interest in the use of magnesium-containing silicate bioceramics such as akermanite, bredigite, merwinite, monticellite, and etc. [14]. Among these bioceramics, monticellite has the higher amount of magnesium in the structure which is about 33%. It has been indicated that the released ions from the constructs made of monticellite could significantly enhance osteoblast adhesion and directly stimulate osteoblast proliferation [14–16].

This class of bioceramics has been frequently reported to be synthesized through sol–gel method from the polycondensation of tetraethyl orthosilicate (TEOS) with nitric acid, which has some limitations, such as increasing the time and temperature of the drying gel, increasing the heat-treatment temperature to archive the final phase, and further milling processes for achieving particles in the range of nanometers (less than 100 nm) [17–19]. Chen et al. [20] have recently proposed a sol–gel-derived synthesis route for the preparation of monticellite bioceramics using nitric acid, that further sintered at 1480°C for 6 h. Although they have reported on the formation of a mono-phase monticellite at the end, their synthesis method was time consuming at higher temperatures.

In this study, monticellite nanoparticles were successfully synthesized by a novel sol–gel method in the presence of ethanol as a precipitant. The high-pure and single-phase monticellite bioceramic was obtained after further sintering procedures. The microstructural and physicochemical properties of the synthesized samples were investigated using Dynamic light scattering (DLS), X-ray powder diffraction (XRD), and Simultaneously thermal analysis (STA), Scanning electron microscopy (SEM), Brunauer–Emmett–Teller (BET), and Fourier transform infrared spectroscopy (FTIR). It is expected that gel preparation from sol precursors occurs in shorter time periods at room temperature, and sintering temperature desirably reduces to lower temperatures. To the best of our knowledge ethanol has not been used for the synthesis of monticellite yet.

2 Experimental

2.1 Materials and methods

The monticellite nanoparticles were prepared by sol–gel method. For this purpose, calcium nitrate tetrahydrate $(Ca(NO_3)_2.4H_2O)$, magnesium chloride hexahydrate $(MgCl_2.6H_2O)$, TEOS $((C_2H_5O)_4Si)$, and ethanol $(C_2H_5OH$, Green solvent) were used as initial precursors. At first, $Ca(NO_3)_2.4H_2O$ and $MgCl_2.6H_2O$ were mixed with ethanol (mol ratio: $Ca(NO_3)_2.4H_2O/ MgCl_2.6H_2O/ C_2H_5OH=1:1:20$) and stirred for 40 min. The dissolution was started with quickly mixing at the temperature of 80°C. Then, TEOS was added to the solution (mol ratio: $Ca(NO_3)_2.4H_2O/ MgCl_2.6H_2O/ Si(C_2H_5O)_4=1:1:1$) and the mixture was slowly stirred for 3 h to be homogenous and single phase. When polycondensation reactions started, some small molecules release as water or alcohol, by which large molecules containing silicon are formed at the end of the reaction, similar to the polymerization process. As a result, the final gel was formed after completion of the condensation reactions and creation of the stable sol at room temperature (after 12 h). The wet gel was heated for 24 h in an oven at 100°C. In the following, the dried-gel calcined at 700, 1100, and 1200 °C for 2 h, using corundum crucible, in an electric furnace under air atmosphere. Finally, the monticellite nanoparticles powders were prepared in a planetary ball mil (Retsch PM 100, Germany) for 5 h with ball/powder ratio: 10/1 and rotational speed: 250 r.p.m.

2.2 Sample characterization

DLS diagram was used for estimating the particle size of the synthesized monticellite nanoparticles (NANOPHOX 90–246 V, Germany). The powders were also analyzed by XRD with X'pert Pro PW 3040-Pro, panalytical. This device was operated with current and voltage setting of 40 mA and 40 KV, respectively, and uses CuKα radiation wavelength (1.540598 Å) in the 2θ rang of 10–80°. It is worth mentioning that the monticellite XRD patterns were analyzed using the X'Pert HighScore Plus software of version 2.2 and through compared with the standard XRD pattern of American Society for Testing and Materials (ASTM International). The thermal behavior of the dried-gel was studied by simultaneously thermal analysis (STA

504 PC/PG, Bähr, Germany) that covers the thermal range between ambient temperature up to 1177.263 °C with the heating rate of 5°C min^{-1}. The microstructure of the synthesized samples was evaluated using SEM. For this purpose, the sample was coated with a thin layer of gold (Au) by sputtering (EMITECH K450X, England) and then the morphology of them observed on a SEM (VEGA/TESCAN, Czech Republic) that operated at the acceleration voltage of 30 kV. Also, Energy dispersive X-ray analyzer (EDS) (Rontec, Germany) connected to the SEM was used to investigate semi-quantitativelychemical compositions. The textural characteristics of the final powder was measured by the BET and Barrett–Joyner–Halenda (BJH) methods (BELSORP Mini, Microtrac Bel Corp, Japan). The powders were also characterized by FTIR (SHIMADZU 8400 S, Japan). For this analysis, 1 mg of the powder samples were carefully mixed with 300 mg of KBr (infrared grade) and pelletized under vacuum. Then, the pellets were analyzed in the range of 400 to 4000 cm^{-1} at the scan speed of 23 scan/min with 4 cm^{-1} resolution.

3 Results and discussion

3.1 Ternary CaO-MgO-SiO$_2$ system

According to the general formula of monticellite (CaMgSiO$_4$), the molar ratio between the metal oxides CaO:MgO:SiO$_2$ is equal to 1:1:1. The monticellite chemical composition is calculated as follows:

$$1CaO + 1MgO + 1SiO_2 = 3$$

$$(100 \times 1)/3 = 33.33\% \, CaO,$$

$$(100 \times 1)/3 = 33.33\% \, MgO,$$

$(100 \times 1)/3 = 33.33\% \, SiO_2$, shown in Fig. 1(a). The suggested ternary plot of this system presented in Fig. 1(b).

3.2 Determination of particles size distribution

In this study, DLS was used to display the size of monophase particles of the synthesized monticellite. The DLS diagram of the synthesized monticellite ceramic at 1200°C are shown in Fig. 2. The distribution of particle size is narrow and most of the particles size is ~85 nm. Some recent studies show that nanoparticles compared to micro-sized particles have superior advantages such as improvement in the biomineralization process, and enhancement in the proliferation and adhesion in contact with cells [21]. The synthesized powders with ethanol have shown particle sizes
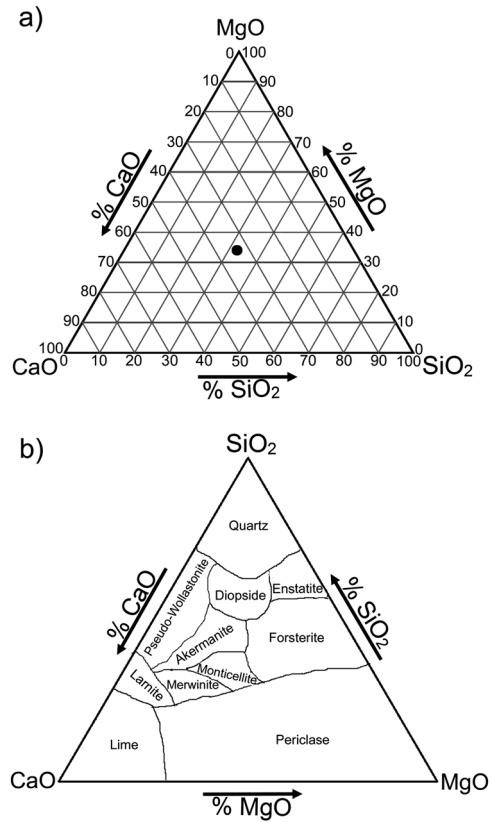

Fig. 1 Ternary phase diagrams; a chemical composition of monticellite, and b schematic showing of the synthesized monticellite zone
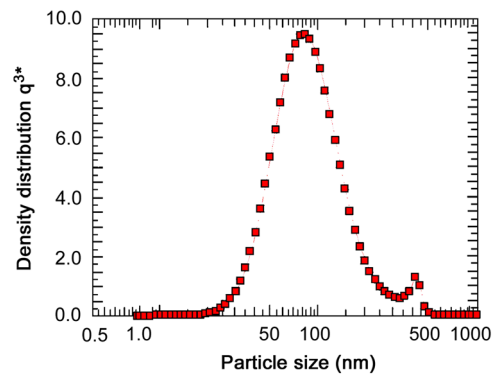

Fig. 2 Distribution diagram of particles size of monticellite ceramic powders

below 100 nm with 5 h ball milling process, while powders synthesized via conventional methods using nitric acid usually need further ball milling processes to achieve nano-sized particles [20, 22].

3.3 Microstructural analysis

Figure 3 shows the XRD patterns of the synthesized monticellite nanoparticles, prepared by sol-gel method, after
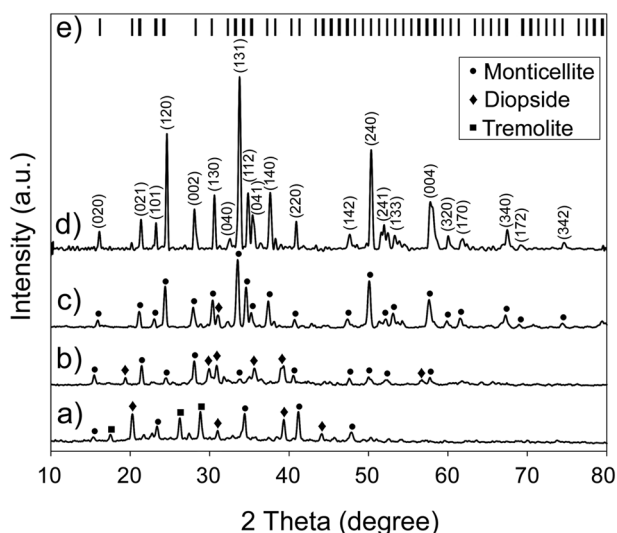
Fig. 3 XRD patterns of the synthesized monticellite nanoparticles after **a** 100 °C **b** 700 °C **c** 1100 °C **d** 1200 °C heat-treatment, and **e** JCPDS Card File No. 01-084-1321

Table 1 Structural parameters of the synthesized monticellite nanoparticles at different temperatures

Sample	D crystallite size (nm)	Lattice parameter (nm)			ε Lattice strain	S Lattice stress (GPa)
		a	b	c		
100°C	28.93	0.4802	1.1017	0.6213	0.001125	0.05737
700°C	18.73	0.4867	1.1224	0.6105	0.003950	0.20145
1100°C	30.96	0.4822	1.1100	0.6386	0.001425	0.07267
1200°C	28.93	0.4793	1.0986	0.6356	0.001575	0.08032

heat-treatment at different temperatures 100, 700, 1100, and 1200 °C. As shown in this figure, the XRD pattern for the dried-gel at 100°C demonstrated that the sample was fully crystalline without any amorphous phases. The dried-gel sintered at the temperature of 1200 °C was pure and single-phase monticellite, while the samples sintered at the temperatures below 1200°C, had some impurities such as diopside ($CaMgSi_2O_6$) and tremolite ($CaMg_3Si_3O_{12}$) along with the monticellite phase. The XRD patterns of the samples sintered at 1100 and 1200°C indicated a sharp peak for monticellite around 33°, which is the main characteristic peak for standard monticellite, according to JCPDS reference card#: 01-084-1321. Three strong peaks diffraction of planes (131), (120), and (240) were also detectable for the monticellite with orthorhombic crystal structure. As can be seen, the synthesized monticellite nanoparticles with ethanol reached the final high-pure phase ($CaMgSiO_4$) at 1200°C, but the synthesized monticellite using conventional methods (for example nitric acid) reached the final phase at 1480°C, indicating that our novel synthesis method is more efficient and cost effective [20]. The mean grain size was also estimated from the half-width of three diffraction peaks with the highest intensity using Debye Scherrer's Eq. (1) [23]:

$$D = k\lambda / \beta \cos \theta \quad (1)$$

It is known that the β used in this formula can be obtained from the difference between the calculated β and β of the device in Eq. (2):

$$\beta = \beta_{Measured} - \beta_{device} \quad (2)$$

Where D is the grain diameter, k is a shape factor (about 0.9), λ is the wavelength for cu-k$_\alpha$ (1.540598 Å),

β is peak width at half maximum intensity, and θ is the X-ray diffraction angle. The monticellite synthesized at 1200°C showed an average crystallite size of nearly 28 nm, in which the average pores size was about 6 nm using BET test. The detail of the microstructural characteristics of different samples after heat-treatment are shown in Table 1.

The crystal lattice parameters can be obtained from determination of the exact position of the reflected peaks. Bragg's law in Eq. (3) provides us with information about crystallographic planes spacing. Then, after using the relation between plane spacing in orthorhombic structure, the lattice constant values can be calculated in Eq. (4).

$$\lambda = 2d_{hkl} \sin \theta \quad (3)$$

$$1/d_{hkl}^2 = h^2/a^2 + k^2/b^2 + l^2/c^2 \quad (4)$$

The enhancement of heat-treatment temperature and its relationship with the changes in lattice constant is shown in Fig. 4. It should be mentioned that the determined lattice parameter for the synthesized monticellite nanoparticles sintered at 1200°C was $a = 0.4793$ nm, $b = 1.0986$ nm and $c = 0.6356$ nm, which was close to its value in the reference card $a_0 = 0.4812$ nm, $b_0 = 1.105$ nm and $c_0 = 0.6364$ nm, shown in Table 1. According to the explanations, monticellite unit cell was orthorhombic, with a space group of pbnm with the number of 61 (JCPDS Card File No. 01-084-1321). The optimum placement of monticellite atoms in one face of unit cell is shown in Fig. 5.

3.4 Average lattice stress and micro-strain calculations

The XRD patterns obtained from the samples showed a deflection from the reference patterns due to the lattice stress/strain. Generally, when a sample is synthesized with lower lattice strain, the yield stress is always in higher values. The micro-strain was determined from the half-width of five diffraction peaks with the highest intensity
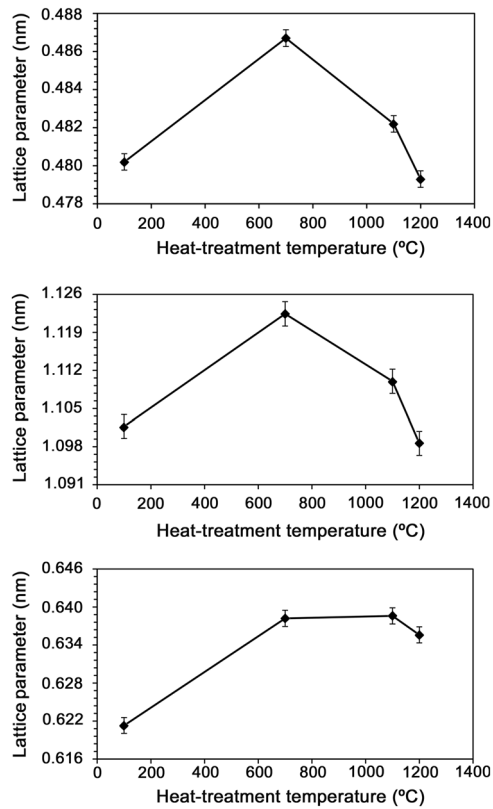
Fig. 4 The relationship between lattice constant changes with heat-treatment temperature for the synthesized monticellite nanoparticles

using the Williamson–Hall Eq. (5) [24]:

$$\beta \cos\theta = k\lambda/D + 4\varepsilon \sin\theta \qquad (5)$$

Warren [25] showed that the β can be calculated using the following formula in Eq. (6):

$$\beta = \sqrt{\beta_{Measured}^2 - \beta_{device}^2} \qquad (6)$$

Where β is the full width at half maximum of the peak, λ is the X-ray wavelength (1.540598 Å) and ε is micro-strain. The $\beta cos\theta/sin\theta$ diagram is shown in Fig. 6, in which the micro-strain was calculated from the slope diagram, and the average nanocrystallite size was measured from the intercepts (the intersection with the vertical axis) diagram. Thus, after extracting the strain (ε) from Williamson–Hall formula, lattice stress could be calculated using Hooke's Law in Eq. (7) [26]:

$$s = Ee \qquad (7)$$

In this representation, the relation between true strain (ε) and engineering strain (e) is $\varepsilon = ln(1 + e)$ that is, if e < 0.01 is e ~ ε, E is the Young's modulus or modulus of elasticity (for monticellite 51 GPa [20]). The lattice stress and strain occurred probably due to crystallographic defects (For example: point defects, line defects, planar defects, and bulk
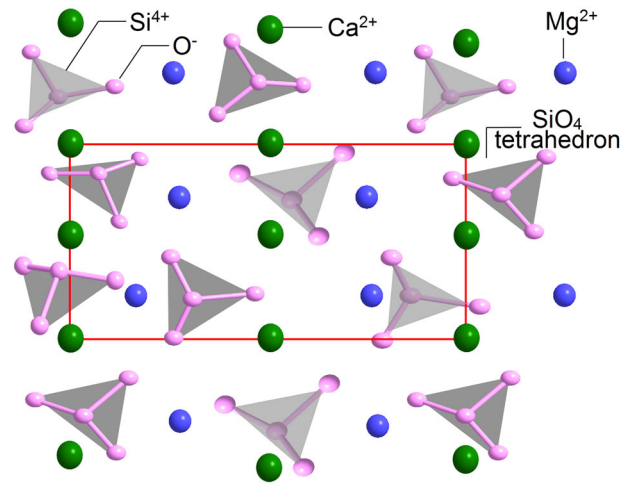

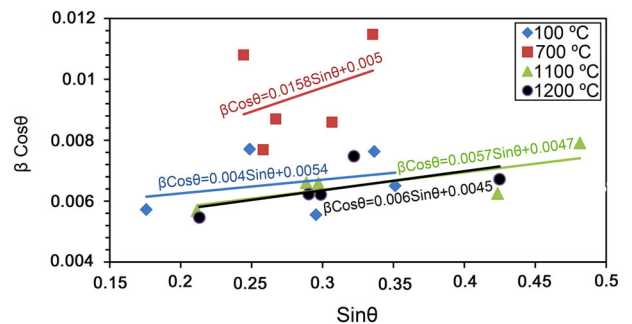Fig. 5 Schematic of one face of the monticellite crystal lattice

Fig. 6 Williamson–Hall diagram of the synthesized monticellite nanoparticles after heat-treatment at different temperatures

defects). In fact, the powder sintered at 1100°C had a lower lattice stress value compared to the powder sintered at 700°C, which might be due to the burning effect of hydrocarbon compounds and their eliminations from the structure. The other reason might be due to the transformation of a multiphase compound (impurities) into monticellite monophase. Therefore, the lattice stress value decreased at the temperature of 1100°C and then increased at 1200°C which could be due to the crystal defects in the monticellite structure.

3.5 Thermal behavior analysis

It is known that a detail analysis on the thermal behavior of bioceramics during heat-treatment process can provide valuable information regarding their final characteristics for biological applications. This sort of analyzes can efficiently show how the structure of a bioceramic develops and when the toxic by-products remove from the samples [27]. Therefore, in the present study, thermal analysis was

conducted on the dried samples at 100°C, shown in Fig. 7. As can be seen, there are endothermic peaks in TG-DTA curves that each one is related to a specific reaction. The
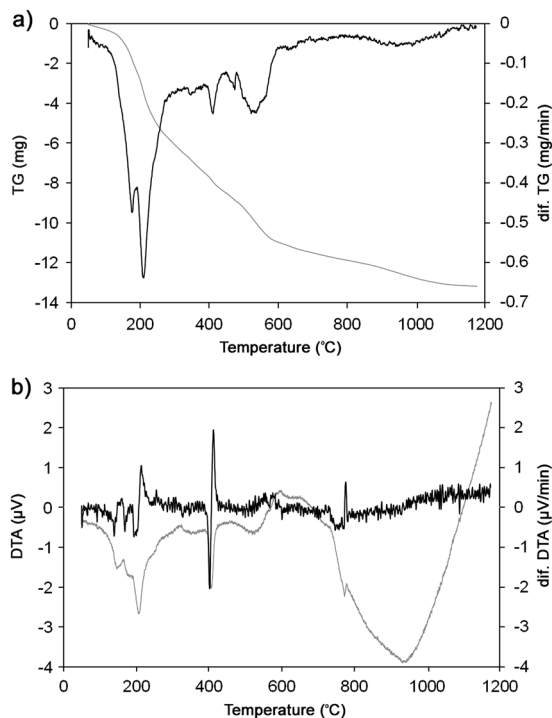

Fig. 7 STA curves of the synthesized monticellite nanoparticles at 100 °C; **a** TG and **b** DTA curves

total mass loss was about 74% related to the drying process during the thermal analysis, which is due to the deletion of different gases from the synthesized monticellite powder. It is worth mentioning that alkyl groups are unstable and combustible after the polycondensation of TEOS which is similar to a polymerization process in low temperature ranges. A major part of the carbon dioxide was removed after the evaporation of water from the microstructure [28]. As can be seen in Fig. 7a, the weight loss rate suddenly increased at about 200°C, and then reached the lowest level at about 1100°C. In another word, it could be also concluded that the elimination of organic and inorganic compounds started at 150°C and continued up to 780°C. The hydrochloric and nitric acid derived from ethanol and metal salts in the gel started to be decomposed by further increasing of the temperature according to the following reaction:

$$HCl + HNO_3 \rightarrow Cl^- + NO_2^+ + H_2O$$
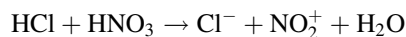
It can be concluded that the products of this decomposition were released from the sample as inorganic gases between 150–780°C. The exothermic peak around 600°C was detected due to the crystallization of monticellite phase.

3.6 Microscopic observations

Figure 8 shows the morphology and chemical composition of the synthesized monticellite nanoparticles. As can be
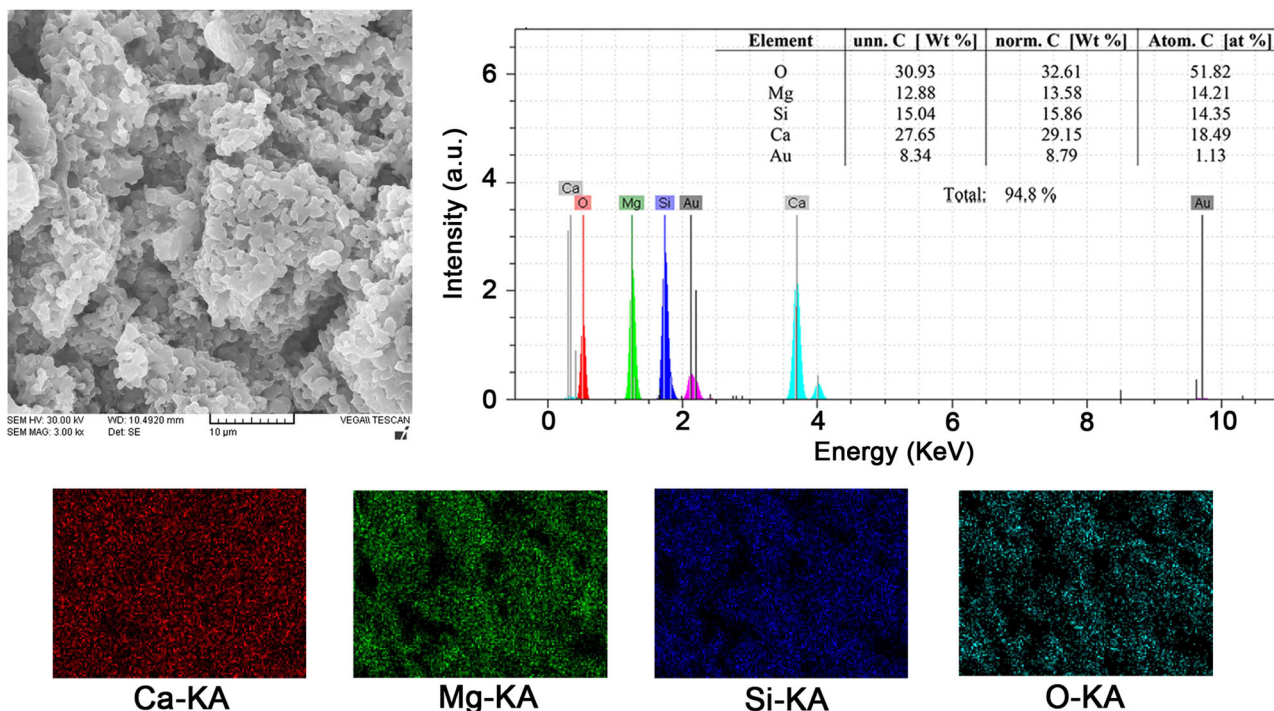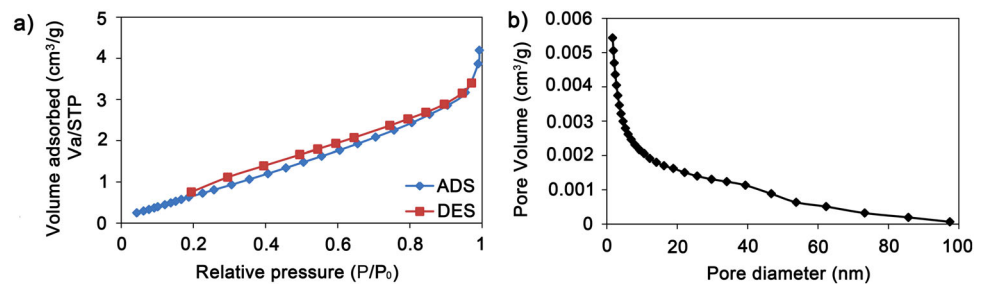

Fig. 8 The typical SEM-EDS and mapping micrographs of the synthesized monticellite nanoparticles sintered at 1200°C

Fig. 9 **a** N$_2$ adsorption/desorption isotherms and **b** BJH pore size distribution from the desorption branch of the synthesized monticellite after heat-treatment at 1200°C for 2 h

seen, there are compact microcrystalline particles composed of small nanoparticles in the range of nano, suggesting that the sintering process forced nanoparticles to be aggregated as larger particles. In addition, the EDS spectra of the nanoparticles confirmed that a monticellite phase was successfully obtained. Moreover, the mapping analysis clearly showed that the Ca, Mg, Si, and O ions were uniformly distributed on the monticellite particles.

3.7 BET and BJH analysis

In the 1985 IUPAC recommendations physisorption isotherms were grouped into six types [29]. However, over the past 30 years various new characteristic types of isotherms have been identified and shown to be closely related to particular pore structures [30]. Figure 9a shows the N$_2$ adsorption–desorption isotherms of the monticellite powders. According to the IUPAC classification, the monticellite ceramic displayed the type III N$_2$ adsorption isotherm at high relative pressure. Hysteresis loop in Fig. 9a is similar to type H3 in the IUPAC hysteresis loops [30, 31]. In the case of a type III isotherm, there is no sharp knee and therefore no identifiable monolayer formation; the adsorbent-adsorbate interactions are now relatively weak and the adsorbed molecules are clustered around the most favorable sites on the surface of a nonporous or macroporous solid [30, 31]. Loops of this type are given by non-rigid aggregates of particles [31]. The result obtained from the adsorption–desorption isotherm by BJH method is shown in Fig. 9b. It was found that the monticellite revealed a thick pore size distribution with a mean pore size of 6.289 nm, a relatively small BET surface area of 4 m^2/g, and the single point adsorption total pore volume (P/P$_0$ = 0.990) of 0.0061 cm^3/g.

3.8 FTIR analysis

The FTIR spectra of the synthesized monticellite nanoparticles at 100, 700, 1100, and 1200°C are shown in Fig. 10. As can be seen, the bond at 3442 cm^{-1} correspond to ν stretching vibration of H$_2$O molecules was detectable for the synthesized powders at 100 and 700°C, which
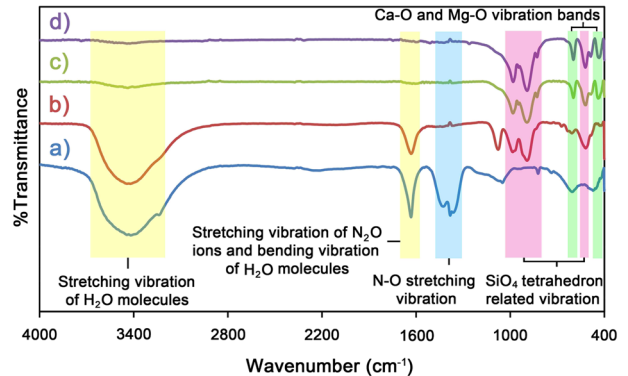

Fig. 10 The FTIR spectra of the synthesized monticellite nanoparticles at different heat-treatment temperatures; **a** 100, **b** 700, **c** 1100, and **d** 1200°C

might be due to the manufactured products of condensation reactions in the sol-gel method and the decomposition reaction of acidic compounds such as HCl and HNO$_3$ to Cl$^-$ and NO$_2^+$ [32]. Moreover, the ν_4, ν_3, and ν_1 stretching vibrations of N–O mode (HNO$_3$) were also detected at 1363, 1382, and 1425 cm^{-1}, respectively, only for the synthesized powders at 100°C [32]. The bond at 1631.67 cm^{-1} correspond to stretching vibration of N=O mode (NO$_2^+$ ions) and δ bending vibration of H$_2$O molecules [32]. A relatively small peak was also observed at 605 cm^{-1} regarding the δ bending vibration of C=O mode for the synthesized powders at 100 and 700°C. In fact, by increasing the heat-treatment temperature, the bands correspond to water, carbon dioxide and nitrate were removed from the structure of the samples. The bonds between 829–981 cm^{-1} and the bond at 520 cm^{-1}, could be seen in all samples, which correspond to the ν stretching vibration and δ bending vibration mode of the SiO$_4$ tetrahedron [33]. These peaks have been more detectable by further heat-treatment of the samples at higher temperatures. To confirm the correct synthesis of monticellite nanoparticles, two main peaks at 433 and 598 cm^{-1} were also detected due to the presence of Mg–O vibration bands [34]. In addition, the band around 423 cm^{-1} indicated the vibration of Ca–O mode [35]. It should be noted that the FTIR spectra of the powders sintered at 1100°C and 1200°C showed similar molecular characteristics.

4 Conclusion

In this paper, a novel synthesis procedure was presented for monticellite nanoparticles in which ethanol and chloride ions accelerated the polycondensation reaction of TEOS during the synthesis process. Ethanol plays the role of a protic green solvent that all precursors were solved in it physically. In the following, after the release of water from the metal salts structure, it starts to react with TEOS. Ethanol can reduce nucleophilicity and rate of condensation effectively through making hydrogen bonds with $\equiv Si{-}O^-$, But on the other hand hydrochloric and nitric acid can be formed as a result due to making hydrogen bonds between ethanol, chloride and nitrate ions (very high nucleophilicity) in solution, Which can reduce the nucleophilicity of $\equiv Si{-}O^-$ less than before. These two mechanisms can cause the stabilization of created complex in sol, reducing the gelling time, creating large molecular networks and formation a transparent gel without crack through controlling the rate of condensation. The effect of hydrochloric or nitric acid anions can only be in non-coordinative electrostatic inter-actions with positively charged as-generated silica particles, which hinder their aggregation in solutions. This procedure showed superior advantages in comparison with the other conventional techniques presented in the literature for the formation of monticellite, which is relatively faster at lower temperatures. In addition, the high-pure monticellite nano-particles were formed in lower temperatures around 1200°C when compared with the conventional techniques which was around 1480°C. The XRD, STA, and FTIR results showed that by further increasing of the temperature, additional materials such as ethanol, carbon dioxide, water, and nitrate were successfully removed from the samples. It is worth mentioning that at 1200°C the sample structure transferred from the multi-phase to single-phase, and finally high-pure monticellite was formed.

Compliance with ethical standards

Conflict of interest The authors declare that they have no competing interests.

References

1. Colombo P (2008) In praise of pores. Science 322(5900):381–383

2. Dapporto M, Sprio S, Fabbi C, Figallo E, Tampieri A (2016) A novel route for the synthesis of macroporous bioceramics for bone regeneration. J Eur Ceram Soc 36(9):2383–2388

3. Deville S (2008) Freeze-casting of porous ceramics: a review of current achievements and issues. Adv Eng Mater 10 (3):155–169

4. Ohji T, Fukushima M (2012) Macro-porous ceramics: processing and properties. Int Mater Rev 57(2):115–131

5. Mozafari M (2014) Bioceramics in the realm of history. Bioceram Dev Appl 4:e106

6. Fukui H, Ohsuka H, Hino T, Kanamura K (2010) A Si−O−C Composite Anode: High Capability and Proposed Mechanism of Lithium Storage Associated with Microstructural Characteristics. ACS Appl Mater Interfaces 2(4):998–1008

7. Saadati MR, Maleki A, Niroumand B, Allafchian AR (2016) A novel low cost method for the synthesis of ceramic nano silicon oxycarbide powder. Ceram Int 42(7):8531–8536

8. Zamanian A, Yasaei M, Ghaffari M, Mozafari M (2013) Calcium hydroxide-modified zinc polycarboxylate dental cements. Ceram Int 39(8):9525–9532

9. Azami M, Jalilifiroozinezhad S, Mozafari M, Rabiee M (2011) Synthesis and solubility of calcium fluoride/hydroxy-fluorapatite nanocrystals for dental applications. Ceram Int 37(6):2007–2014

10. Dutta S, Passi D, Singh P, Bhuibhar A (2015) Ceramic and non-ceramic hydroxyapatite as a bone graft material: a brief review. Ir J Med Sci 184(1):101–106. (1971)

11. Ramedani A, Yazdanpanah A, Moztarzadeh F, Mozafari M (2014) On the use of nanoliposomes as soft templates for controlled nucleation and growth of hydroxyapatite nanocrystals under hydrothermal conditions. Ceram Int 40(7):9377–9381

12. Ghaffari M, Moztarzadeh F, Sepahvandi A, Mozafari M, Faghihi S (2013) How bone marrow-derived human mesenchymal stem cells respond to poorly crystalline apatite coated orthopedic and dental titanium implants. Ceram Int 39 (7):7793–7802

13. Dietrich E, Oudadesse H, Lucas-Girot A, Mami M (2009) In vitro bioactivity of melt-derived glass 46S6 doped with magnesium. J Biomed Mater Res A 88(4):1087–1096

14. Diba M, Goudouri O-M, Tapia F, Boccaccini AR (2014) Magnesium-containing bioactive polycrystalline silicate-based ceramics and glass-ceramics for biomedical applications. Curr Opin Solid St M 18(3):147–167

15. Webster TJ, Ergun C, Doremus RH, Bizios R (2002) Hydro-xylapatite with substituted magnesium, zinc, cadmium, and yttrium. II. Mech osteoblast Adhes J Biomed Mater Res 59(2):312–317

16. Liu C, Yeh J, Aloia J (1988) Magnesium directly stimulates osteoblast proliferation. J Bone Miner Res 3:S104

17. Wu C, Chang J (2004) Synthesis and apatite-formation ability of akermanite. Mater Lett 58(19):2415–2417

18. Wu C, Chang J, Wang J, Ni S, Zhai W (2005) Preparation and characteristics of a calcium magnesium silicate (bredigite) bioac-tive ceramic. Biomaterials 26(16):2925–2931

19. Hafezi-Ardakani M, Moztarzadeh F, Rabiee M, Talebi AR (2011) Synthesis and characterization of nanocrystalline merwinite (Ca 3 Mg (SiO 4) 2) via sol–gel method. Ceram Int 37(1):175–180

20. Chen X, Ou J, Kang Y, Huang Z, Zhu H, Yin G, Wen H (2008) Synthesis and characteristics of monticellite bioactive ceramic. J Mater Sci Mater Med 19(3):1257–1263

21. Yazdanpanah A, Kamalian R, Moztarzadeh F, Mozafari M, Ravarian R, Tayebi L (2012) Enhancement of fracture toughness in bioactive glass-based nanocomposites with nanocrystalline forsterite as advanced biomaterials for bone tissue engineering applications. Ceram Int 38(6):5007–5014

22. Razavi M, Fathi M, Savabi O, Beni BH, Vashaee D, Tayebi L (2014) Surface microstructure and in vitro analysis of nanos-tructured akermanite (Ca 2 MgSi 2 O 7) coating on biodegradable

magnesium alloy for biomedical applications. Colloid Surf B 117:432–440

23. Mozafari M, Moztarzadeh F, Vashaee D, Tayebi L (2012) Effects of heat treatment on physical, microstructural and optical characteristics of PbS luminescent nanocrystals. Phys E 44 (7):1429–1435

24. Ganjali M, Pourhashem S, Mozafari M (2015) The effect of heat-treatment on the structural characteristics of nanocrystalline chlorapatite particles synthesized via an in situ wet-chemical route. Ceram Int 41(10):13100–13104

25. Warren BE (1969) X-ray Diffraction. Courier Corporation, New York

26. Dieter GE (1988) Mechanical metallurgy. McGraw-Hill Book Company, UK, vol SI Metric edn

27. Mozafari M, Moztarzadeh F, Tahriri M (2010) Investigation of the physico-chemical reactivity of a mesoporous bioactive SiO 2–CaO–P 2 O 5 glass in simulated body fluid. J Non-Cryst Sol 356(28):1470–1478

28. Iwata NY, Lee G-H, Tsunakawa S, Tokuoka Y, Kawashima N (2004) Preparation of diopside with apatite-forming ability by sol–gel process using metal alkoxide and metal salts. Colloid Surf B 33(1):1–6

29. Sing K, Everett D, Haul R, Moscou L, Pierotti R, Rouquerol J, Siemieniewska T (1985) Physical and biophysical chemistry division commission on colloid and surface chemistry including catalysis. Pure Appl Chem 57(4):603–619

30. Lowell S, Shields JE, Thomas MA, Thommes M (2012) Characterization of porous solids and powders: surface area, pore size and density, vol 16. Springer Science & Business Media, Dordrecht

31. Rouquerol J, Rouquerol F, Llewellyn P, Maurin G, Sing KS (2013) Adsorption by powders and porous solids: principles, methodology and applications. Academic press, Oxford, UK

32. Taibi M, Ammar S, Jouini N, Fiévet F, Molinié P, Drillon M (2002) Layered nickel hydroxide salts: synthesis, characterization and magnetic behaviour in relation to the basal spacing. J Mater Chem 12(11):3238–3244

33. Li K, Fan J, Shang M, Lian H, Lin J (2015) Sr 2 Y 8 (SiO 4) 6 O 2: Bi 3+/Eu 3+: a single-component white-emitting phosphor via energy transfer for UV w-LEDs. J Mater Chem C 3 (38):9989–9998

34. Niu H, Yang Q, Tang K, Xie Y (2006) Large-scale synthesis of single-crystalline MgO with bone-like nanostructures. J Nanopart Res 8(6):881–888

35. Imtiaz A, Farrukh MA, Khaleeq-ur-Rahman M, Adnan R (2013) Micelle-assisted synthesis of Al2O3·CaO nanocatalyst: optical properties and their applications in photodegradation of 2, 4, 6-Trinitrophenol. Sci World J. doi:10.1155/2013/641420